J. Ilsemann, A. Sonström, T. M. Gesing, R. Anwander, M. Bäumer

Highly Active Sm2O3-Ni Xerogel Catalysts for CO2 Methanation

Journal Article as: peer-reviewed accepted version (Postprint)

DOI of this document*(secondary publication): https://doi.org/10.26092/elib/2479

Publication date of this document: 22/09/2023

* for better findability or for reliable citation

Recommended Citation (primary publication/Version of Record) incl. DOI:

J. Ilsemann, A. Sonström, T. M. Gesing, R. Anwander, M. Bäumer,
Highly Active Sm2O3-Ni Xerogel Catalysts for CO2 Methanation
ChemCatChem 2019, 11, 1732
https://doi.org/10.1002/cctc.201802049

DOI: 10.1002/cctc.201802049

Highly Active Sm_2O_3-Ni Xerogel Catalysts for CO_2 Methanation

Jan Ilsemann[+],[a] Andrea Sonström[+],[b] Thorsten M. Gesing,[c, d] Reiner Anwander,[b] and Marcus Bäumer*[a, d]

We report on a new synthesis route for pure Sm_2O_3 and Sm_2O_3-Ni xerogels by modifying the well-known epoxide addition method. The resulting xerogels are used to prove the suitability of samaria as a highly effective catalyst support and to determine the optimal Ni loading. Therefore, a set of five catalysts with Ni loadings between 4 wt% and 89 wt% Ni was prepared and fully characterized by X-ray diffraction, N_2 physisorption, transmission electron microscopy and H_2 temperature-programmed reduction. Catalytic measurements reveal that the catalyst with 39 wt% Ni shows the best catalytic performance, outperforming even highly active literature known systems. Stability runs indicate that the catalyst deactivates independently of the Ni loading as well as conversion level over 600 min due to, most likely, carbonate formation. This deactivation, however, is reversible by a simple regeneration step. As shown by simultaneous CO_2/CO methanation measurements, the Ni–Sm_2O_3 catalysts are also highly efficient for CO methanation. In this case, CO is preferentially converted to methane compared to CO_2.

Introduction

Future energy systems will rely heavily on renewable energies. Their fluctuating nature, in turn, generates an urgent need for suitable energy storage systems to ensure a reliable power supply. When using hydrogen from electrolysis, one concept often discussed as a potential answer is the Power-to-Gas technology (PTG), in which methane is produced from carbon containing educts such as CO and CO_2. When using CO_2 as feedstock, the highly exothermic reaction follows the stoichiometric equation below [Eq. (1)]:

$$CO_2 + 4\ H_2 \leftrightarrow CH_4 + 2\ H_2O \qquad \Delta H_R^{298K} = -165\ kJ\ mol^{-1} \qquad (1)$$

The reaction is usually catalyzed by supported transition metals, mainly Fe, Ni and Co,[1–3] of which, due to its high activity and methane selectivity, nickel is the most common catalyst. Cobalt performs similarly, however, comes at a higher price, whereas, Fe has a high activity but a poorer methane selectivity.[4] Ruthenium is widely regarded as the most active metal,[5] but its high price renders an industrial application uneconomic. Conventional systems usually use Al_2O_3, SiO_2 or TiO_2 as supports, as they offer high surface areas for accommodating the small metal particles.[3] While mechanistically it is still debated if the reaction proceeds by an associative or a dissociative route, both strands assume CO_2 adsorption on the metal-support perimeter, showing that the support plays an important role during the reaction.[6–8] Several studies compare different support materials regarding their impact on activity and selectivity.[9–11] Nickel supported on alumina is the most common system; however, it faces a few drawbacks due to its propensity to coking as well as sintering. Furthermore, phase composition is difficult to control and the catalytically inactive and hardly reducible spinel phase $NiAl_2O_4$ readily forms during calcination at higher temperatures when small Ni particles are present.[12–14] In turn, silica-supported systems suffer from their acidic surface properties which hamper CO_2 adsorption as well as lead to severe coking problems.[15] Therefore, recent research has shifted towards new, more unconventional systems. Here, rare earth metal oxides (REOs) have been considered as suitable catalyst supports, while they have long been used as dopants. It is known that La_2O_3 increases Ni dispersion as well as H_2 uptake,[16] whereas, CeO_2 has been shown to increase both the catalyst stability as well as reducibility.[17] REOs usually exhibit basic surface properties[18] which should improve the activity of the catalyst due to a stronger CO_2 adsorption.[19] Aldana et al.,[6] for example, attributed the better performance of a ceria-zirconia supported catalyst compared to a Ni-SiO_2 catalyst to its higher basicity. Tada et al.[20] compared various Ni systems and achieved the highest activity for Ni–CeO_2, an observation they attributed to the high amount of adsorbed CO_2 as shown by CO_2-TPD measurements. Atzori et al.[21] prepared Ni–CeO_2 catalysts with various metal loadings by a hard-template

[a] J. Ilsemann,[+] Prof. Dr. M. Bäumer
University of Bremen
Institute of Applied and Physical Chemistry
28359 Bremen (Germany)
E-mail: mbaeumer@uni-bremen.de
[b] A. Sonström,[+] Prof. Dr. R. Anwander
University of Tübingen
Institute of Inorganic Chemistry
72076 Tübingen (Germany)
[c] Prof. Dr. T. M. Gesing
University of Bremen
Institute of Inorganic Chemistry and Crystallography
28359 Bremen (Germany)
[d] Prof. Dr. T. M. Gesing, Prof. Dr. M. Bäumer
University of Bremen
MAPEX Center for Materials and Processes
28359 Bremen (Germany)
[+] These authors contributed equally to the work.

Supporting information for this article is available on the WWW under https://doi.org/10.1002/cctc.201802049

method which uses SBA-15 to adjust the pore size. They found their systems to be very active and linked the high activity to the nickel-ceria interaction. Sharma et al.[22] used ruthenium doped ceria as a catalyst and achieved a high activity as well as selectivity. In comparison to CeO_2 and La_2O_3, Sm_2O_3 has received only little attention as a suitable catalyst support or promoter for CO_2 methanation. Muroyama et al.[10] prepared several Ni catalysts by impregnating conventional supports such as Al_2O_3 as well as several rare earth metal oxides and found that the 10 wt% Ni–Sm_2O_3 system outperforms conventional systems in the low-temperature regime. However, the catalyst was prone to a rapid deactivation which could not be explained by sintering or coking. In terms of stability, particularly for high temperature reactions, xerogel catalysts are a promising, yet seldom investigated alternative as compared to impregnated and precipitated catalysts. The homogenous sol-gel approach allows a strong interaction of the support and the active component due to a partial encapsulation usually resulting in a high sinter stability.[23]

In this paper, we (a) establish a new one-pot synthesis route for the preparation of Ni loaded samaria xerogel catalysts, which complements the propylene oxide method,[24] show that (b) these systems provide a high thermal stability and are (c) highly efficient catalysts for CO_2 methanation. By varying the composition, we aim at investigating the effect of the nickel loading on the structural properties as well as their catalytic performance to clarify whether samaria should rather be used as a catalyst support (large amount) or a promoter (small amount). The materials have been fully characterized by N_2 physisorption, H_2-TPR, XRD as well as TEM. We can show that an optimal Ni–Sm_2O_3 ratio exists and, furthermore, demonstrate, by comparing our catalytical data to the reference kinetics of a highly active, literature-known system, the potential of Ni–Sm_2O_3 systems for CO_2 methanation. Also, simultaneous CO_2/CO methanation experiments were carried out to prove the high activity for a variety of applications, such as coke oven gas methanation, and to also gain indirectly mechanistic insight.

Experimental

Synthesis

Samaria/nickel xerogels with 4, 11, 39, 63 and 89 wt% Ni^0 loading were prepared following a procedure, which is based on the PO (propylene oxide)-method developed by Gash et al.[24] First, Sm $(NO_3)_3$*xH_2O (Chempur, 99.9%) and Ni$(NO_3)_2$*6 H_2O (Sigma Aldrich, 98.5%) were dissolved in absolute ethanol (1.7 g ethanol/1 mmol metal salt) under stirring in a polyethylene vial. Next, citric acid (CA, Roth, 99.5%, anhydrous) was added (1 mmol CA per 1 mmol metal salt). Once dissolution was complete, propylene oxide (Aldrich, 99.5%), as a gelation initiator (11 mmol of PO/1 mmol of metal salt), was quickly added to the mixture. The resulting solution was stirred, while gelation occurred rapidly within a few seconds, independently of the composition. The formed gel was allowed to age undisturbed for at least 24 hours. To remove any residues of the synthesis, a solvent exchange with pure ethanol was conducted three times by decanting the old solvent. Ambient drying for at least five days yielded xerogels, which were subsequently calcined in air at 873 K (heating ramp 1 K/min) for 2 hours. The respective amounts used to synthesize 1 g of catalyst are summarized in Table 1.

Table 1. Calculated amounts of precursors.

	Ni $(NO_3)_2$*6H_2O [g]	Sm $(NO_3)_3$*xH_2O [g]	Ethanol [mL]	Propylene Oxide [mL]	Citric acid [g]
Pure Sm_2O_3	–	2.20	9.9	3.8	0.95
4 wt% Ni	0.20	2.06	10.6	4.1	1.02
11 wt% Ni	0.55	1.95	12.5	4.8	1.20
39 wt% Ni	1.93	1.34	19.3	7.4	1.86
63 wt% Ni	3.12	0.81	25.1	9.7	2.41
89 wt% Ni	4.41	0.24	30.8	11.9	2.96

Characterization

N_2 physisorption. The specific surface area of the calcined samples was determined by five-point BET measurements in the pressure range 0.1–0.3 P/P_0 using a NOVA 4000e (Quantachrome Instruments, USA) gas sorption system. Additionally, adsorption/desorption isotherms were collected in the pressure range 0.01–0.99 P/P_0. The pore size distribution was calculated from the desorption branch by the Barret-Joyner-Halenda (BJH) model, while the pore volume was determined at $P/P_0 = 0.99$. Prior to data collection, the samples were outgassed at 473 K for at least 2 hours under vacuum. All measurements were conducted at 77 K.

H_2 temperature-programmed reduction. To determine the optimal reduction temperature and to gain insights into the metal-support interaction, temperature-programmed-reduction (TPR) profiles were recorded, using an Autosorb I (Quantachrome Instruments, USA) device equipped with a TCD detector. The samples (75 mg) were pre-treated at 673 K for 10 h under flowing He to remove any adsorbed impurities. After cooling the samples down to 323 K, the cell was purged with He until a steady TCD signal was observed and subsequently heated to 1273 K with a linear heating ramp of 5 K/min in 5% H_2/Ar.

Powder XRD. The freshly prepared xerogel powders were characterized by XRD to identify and quantify the phases present as well as to calculate the average crystallite sizes. The samples were measured using a $\theta/2\theta$-Bragg-Brentano geometry on a X'Pert MPD powder diffractometer (Panalytical, Almelo, Netherlands). The instrument was equipped with a secondary Ni filter, Cu $K_{\alpha1,2}$ radiation ($\lambda_1 = 154.05929(5)$ pm, $\lambda_2 = 154.4414(2)$ pm), and an X'Celerator multi-strip detector. Data were collected at ambient condition in the 2θ range from 15° to 90° with a step width of 0.0167°/step and a total collection time of 200 s/step. X-ray powder data Rietveld refinements were carried out, using the "DiffracPlus Topas 4.2" software (Bruker AXS GmbH, Karlsruhe, Germany). To describe the X-ray diffraction profiles, the fundamental parameter approach was applied in the Rietveld refinements. For the diffractometer configuration, the corresponding fundamental parameters were fitted to powder data of standard LaB_6. During the refinements, general parameters, such as scale factors and background parameters (Chebychev polynomial), were optimized. Additionally, the lattice parameters, atomic coordinates, isotropic atomic displacement parameters, average crystallite size L_{vol}(IB) and microstrain (ε_0) were refined.

TEM. TEM images were acquired from the powders with a Tecnai F20S-TWIN (200 keV) microscope, equipped with an EDX detector to gain insight into the catalyst microstructure.

Catalysis

Catalytic tests were conducted under atmospheric pressure in a fixed-bed reactor to compare the activity and selectivity of each sample. To this end, a quartz glass tube reactor with an inner diameter of 6 mm was filled with 50 mg of the powder catalyst (75–200 μm) and diluted with 300 mg Al_2O_3 consisting of particles in the same fraction. Quartz wool was used to fix the powder inside the reactor. The total flow rates remained fixed at 50 mL_N/min with the following feed composition: $H_2/CO_2/Ar = 4/1/5$. Gas flow rates were controlled by mass flow controllers (Bronkhorst Mättig). The catalysts were tested between 473–673 K in intervals of 50 K. Therefore, a self-designed metal block oven was used, the temperature of which was controlled by a thermocouple, placed at the reactor wall. Each temperature was held for 42 minutes during which the catalytic performance was monitored with an on-line compact gas chromatograph (Global Analyser Solution) equipped with a thermal conductivity detector. A RT-Molsieve 5 Å column (15 m) was used to detect CO and CH_4, whereas CO_2 was detected on a RT-Porabond column (30 m). CO_2 conversion (X_{CO2}) as well as CH_4 yield (Y_{CH4}) and selectivity (S_{CH4}) were determined by using an external standard and according to the following equations [Eqs. (2)–(4)]:

$$X_{CO_2} = 1 - \frac{c_{CO_2,out}}{c_{CO_2,out} + c_{CH_4,out} + c_{CO,out}}, \quad (2)$$

$$Y_{CH_4} = \frac{c_{CH_4,out}}{c_{CO_2,out} + c_{CH_4,out} + c_{CO,out}}, \quad (3)$$

$$S_{CH_4} = \frac{Y_{CH_4}}{X_{CO_2}}. \quad (4)$$

Pre-experiments confirmed the absence of any higher hydrocarbons. Prior to the reaction, the catalysts were reduced in-situ in flowing H_2 at 773 K for 10 h (heating ramp 1 K/min). After reduction, the reactor was cooled down in inert gas atmosphere. To avoid condensing of water inside the set-up, all tubing was heated.

As a reference, we used a micro kinetic model available in literature, which was implemented in an isothermal 1D pseudo-homogenous reactor model, assuming ideal conditions, e.g. no inter- or intra-particle diffusion limitations, such that only the mass balance [Eq. (5)] had to be solved numerically.

$$\frac{d\dot{n}_i}{dm} = \nu_i \cdot r \quad (5)$$

Choosing the reaction conditions according to our experimental conditions enabled a direct comparison of the catalytic performance under identical conditions. To this end, the rate expression of Koschany et al.[25] was employed without any alterations [Eq. (6)].

$$r = \frac{k \cdot p_{H_2}^{0.5} p_{CO_2}^{0.5} \cdot \left(1 - \frac{p_{CH4} p_{H_2O}^2}{p_{CO2} \cdot p_{H2}^4 \cdot K_{eq}}\right)}{\left(1 + K_{OH} \frac{p_{H_2O}}{p_{H_2}^{0.5}} + K_{H2} p_{H_2}^{0.5} + K_{mix} p_{CO2}^{0.5}\right)^2} \quad (6)$$

Their kinetic parameters are given in Table 2. All adsorption constants K_{OH}, K_{H2} and K_{mix} and the rate constant k are assumed to be of van't Hoff or Arrhenius type, respectively. It must be noted, though, that, prior to the kinetic measurements, Koschany et al. [25] aged their catalyst to avoid deactivation while collecting data for the kinetics, whereas we did not subject our samples to such an aging procedure.

Table 2. Applied kinetic parameters as determined by Koschany et al.[25]

Parameter	value	Parameter	value
k_0	$3.46^{*}10^{-4}$ *mol bar^{-1} s^{-1} g$_{cat}^{-1}$*	A_{H_2}	0.44 *bar$^{-0.5}$*
E_A	77.5 *kJ mol^{-1}*	ΔH_{H_2}	−6.2 *kJ mol^{-1}*
A_{OH}	0.5 *bar$^{-0.5}$*	A_{mix}	0.88 *bar$^{-0.5}$*
ΔH_{OH}	22.4 *kJ mol^{-1}*	ΔH_{mix}	−10 *kJ mol^{-1}*

H_X adsorption enthalpy; A_x corresponding pre-exponential factor; E_A activation energy, k_0 corresponding pre-exponential factor.

Results and Discussion

Synthesis

Our modified "Pechini-PO-method" uses nitrates as precursors, since the use of chloride-precursors (via the well-known PO-method[24]), as established to obtain iron-oxide monoliths, for instance, only resulted in oxychlorides, rather than oxides when applied to rare earth elements.[26] When, instead, using nitrates as precursors, Clapsaddle et al.[26] noted for the classical PO route that no change in pH-value occurs which is a prerequisite for gelation.

Mechanistically, aqua complexes of the corresponding metal cations are formed by dissolving the chloride or nitrate precursors in ethanol. To enable a slow deprotonation of the cation acid (hydrolysis of the rare earth metal salt), propylene oxide is used as a proton scavenger [Eq. (7)].

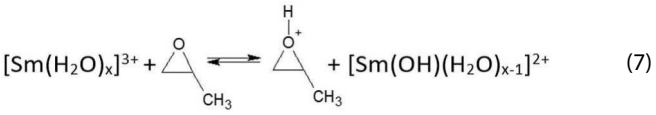

(7)

In case of the chloride precursors this leads to a shift of the equilibrium of reaction (7) to the product side. The chloride anions in solution can easily perform a nucleophilic attack on the protonated propylene oxide and, therefore, irreversibly remove one product out of the equilibrium reaction. Nitrate anions, on the other hand, are bad nucleophiles. Hence, the Lewis acidity of the metal cation becomes the dominant parameter of hydrolysis [Eq. (7)] and condensation [Eq. (8)]

$$2\ [Sm(OH)(H_2O)_{x-1}]^{2+} \rightarrow [(H_2O)_{x-1}SmOSm(H_2O)_{x-1}]^{4+} + H_2O. \quad (8)$$

An enhanced control of the hydrolysis and condensation reaction sequences is achieved in the presence of citric acid as a chelating agent. In the absence of PO, only a white precipitate formed after several days, revealing that no gelation occurs just in the presence of citric acid. According to this synthesis route, five representative catalysts systems with 4, 11, 39, 63 and 89 wt% Ni were prepared and are described in the following sections.

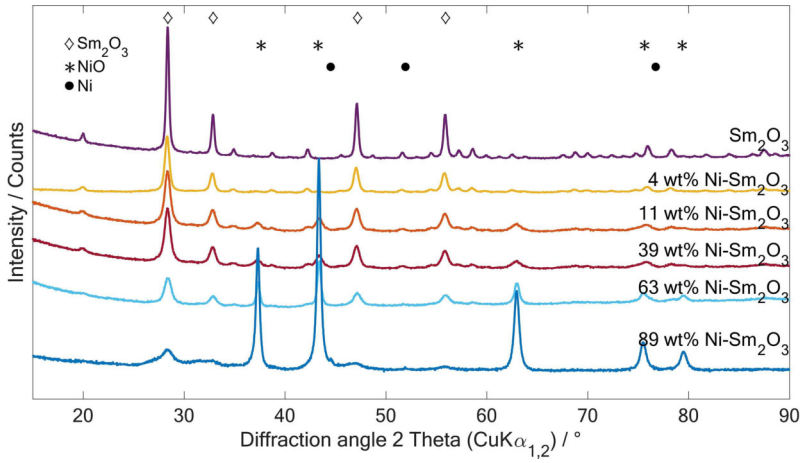

Figure 1. XRD pattern of the prepared xerogels. For a better visibility, only the main peak positions of the different phases are given.

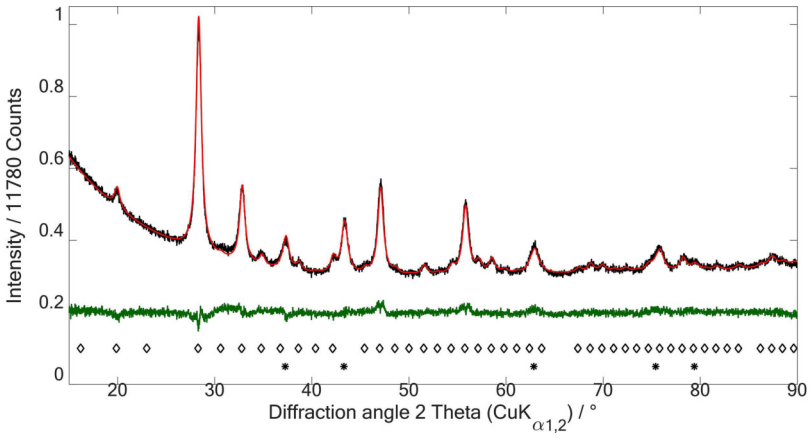

Figure 2. Rietveld plot of 39 wt % Ni–Sm_2O_3; observed pattern in black, calculated pattern in red, difference curve in green. The possible reflection positions of Sm_2O_3 and NiO are given as diamond and asterisk markers, respectively.

PXRD and TEM

All samples were analyzed by powder XRD to quantitatively evaluate their phases as well as to determine crystallite sizes. The results are given in Figure 1. As a reference pure Sm_2O_3 was prepared using the same method. The diffraction patterns were analyzed by Rietveld refinement using the structural models for Ni (space group $Fm\bar{3}m$), NiO (space group $Pm\bar{3}m$) and Sm_2O_3 (space groups $I2_13$ and $Ia\bar{3}$).

Representative results for the refinement of 39 wt % Ni–Sm_2O_3 are depicted in Figure 2.

All diffraction patterns exhibit the typical reflections for A-type Sm_2O_3 ($Ia\bar{3}$) at 28.45°, 32.87°, 47.09° and 55.88° 2 Θ (Cu-radiation). Upon an increasing Ni share, the characteristic diffraction peaks for NiO ($Pm\bar{3}m$) become predominant. The quasi-binary samples can be explained by a combination of the two pure materials, showing no additional peaks, that could be attributed to the unwanted perovskite. The sample 11 wt % Ni–Sm_2O_3 also contains diffraction peaks for C-Type Sm_2O_3 ($I2_13$) at 28.26°, 32.75° and 46.99° 2 Θ meaning that the phase transformation from the disordered to the ordered phase has not been fully accomplished, yet. This would indicate that the calcination duration is at the lower limit to achieve full phase transformation. However, since a second thermal treatment step (reduction of the catalyst) follows, during which residual C-type Sm_2O_3 is transformed into A-type, as could be evidenced by post-reduction XRD measurements (see SI, Figure S1), this finding most likely does not affect the catalytical results. Remarkably, the sample with 89 wt % Ni shows three further peaks, though small, at 44.5°, 51.9° and 76.5° 2 Θ. Zhang[27] synthesized pure NiO films by a sol-gel route based on nickel acetate tetrahydrate and assigns the same peaks to Ni^0 or Ni^{3+}, assuming a disproportionation reaction during the annealing step at 773 K [Eq. (9)].

$$3\ NiO \rightarrow Ni + Ni_2O_3 \qquad (9)$$

Based on our Rietveld refinements, we attribute these reflections to metallic Ni ($Fm\bar{3}m$). Since calcination takes place in air, we believe that the addition of citric acid leads to a

Table 3. Lattice parameters, crystallite sizes L_{Vol}(IB) and NiO loadings as calculated by Rietveld refinement.

wt% Ni in Sm_2O_3	a(NiO) [pm]	a(Sm_2O_3) [pm]	Average crystallite size L_{Vol} (IB) [nm] NiO	Sm_2O_3	NiO [wt%]
4	419(1)	1093(1)	14(1)	13(1)	4.7(1)
11	418(1)	1093(1)	15(1)	10(1)	14.3(1)
39	418(1)	1093(1)	8(1)	9(1)	43.4(1)
63	418(1)	1091(1)	18(1)	8(1)	69.3(1)
89	417(1)	1094(1)	19(1)	6(1)	90.5(1) (0.7(1) Ni)

reducing atmosphere by decomposition to elemental carbon at 873 K. Furthermore, it is noteworthy that the diffraction peaks of the samples containing both NiO and Sm_2O_3 are slightly broadened, indicating a smaller average crystallite size as compared to pure samaria. Table 3 summarizes the calculated lattice parameters, the average crystallite sizes L_{Vol}(IB) as well as the NiO loading of the catalyst. All lattice parameters are in good agreement with the literature.[28,29] The average crystallite size of NiO is in the range of 8 to 19 nm, whereas Sm_2O_3 crystallites are considerably smaller, ranging between 6 and 10 nm. Except for the sample with 39 wt% Ni, the crystallites sizes behave as expected. An increased loading of the respective element also causes an increase in the corresponding average crystallite size and vice versa.

We collected transmission electron micrographs of the various samples after calcination to understand if the particles are single crystalline or multi crystalline. The images as well as a short description are attached in the SI (Figure S2). All samples exhibit a particulate structure as expected for xerogels derived from nitrates.[30] Unfortunately, no clear contrast is visible in the micrographs allowing to distinguish between NiO and Sm_2O_3 particles. Even EDX measurements did not reveal significant variations in the composition which would allow to correlate a certain shape or area with either NiO or Sm_2O_3.

BET/BJH

N_2 physisorption measurements were conducted to obtain information about the catalysts' morphologies in dependence of the Ni loading. The results are shown in Table 4 as well as Figure 3. Except for the sample with the highest Ni loading, the obtained specific surface areas (SSA) follow a trend in that a decreasing SSA is observed with increasing Ni amount.

Table 4. BET/BJH results for the synthesized xerogel powders.

	SSA [$m^2 g^{-1}$]	Pore volume[a] [$cm^3 g^{-1}$]	Max. pore radius distribution[b] [nm]	Average pore radius[b] [nm]
Sm_2O_3	31	0.12	5.1	7.5
4 wt% Ni–Sm_2O_3	28	0.08	4.2	6.2
11 wt% Ni–Sm_2O_3	22	0.06	3.8	5.5
39 wt% Ni–Sm_2O_3	19	0.06	5.1	6.1
63 wt% Ni–Sm_2O_3	9	0.02	1.9	4.7
89 wt% Ni–Sm_2O_3	13	0.05	1.9	8

[a] calculated by the Barret-Joyner-Halenda (BJH) method at $p/p_0 = 0.99$; [b] calculated of the desorption branch using the BJH method.

The specific surface areas are rather small; e.g. Neumann et al.[31] synthesized Sm_2O_3-Al_2O_3 xerogels by a similar route and achieved specific surface areas as high as 117 m^2/g. The smaller surface areas can be explained by the high molar mass of the samaria. When comparing the results to other Sm_2O_3 supported systems, the values are, however, in good agreement with the literature. Zhang et al.[32] found a SSA for a Ni–Sm_2O_3 xerogel prepared by a different route after calcination at 823 K of 8 m^2/g, whereas Gomez-Sainero et al.[33] synthesized Sm_2O_3-CeO_2 powders, which they calcined at 1073 K, with 9.7 m^2/g SSA. Using the IUPAC classification, all samples exhibit, as shown in Figure 3, type IV isotherms indicating mesopores and are, therefore, considered suitable for catalytic applications. Micropores appear to be absent as no steep increase in N_2 uptake is measured at low P/P_0 values. With increasing Ni content, the hysteresis loop changes from H2-type, indicative for porous materials with spherical pores, to H3-type, which is characteristic for slit-shaped pores and plate-like particles. Furthermore, the hysteresis loop decreases in size as well as N_2 uptake at high Ni loadings, indicative for a denser material; accordingly, the pore size distribution is shifted to smaller radii. The derived pore size distributions are rather broad. Additional Hg intrusion porosimetry measurements confirmed the absence of macropores, possibly undetected by N_2 physisorption as shown in Figure S3.

H_2-TPR

H_2-TPR profiles were recorded to study and compare the reducibility as well as the interaction between NiO and Sm_2O_3. Since the XRD results reveal the absence of any mixed phases, only one reduction peak is expected in the scanned temperature regime accounting for the reduction of NiO to metallic Ni. Figure 4 shows the measured profiles. Although all profiles were recorded with around 75 mg of the respective powder, the profiles are scaled by the respective sample mass to allow a better comparison. As the TCD signal of the pure Sm_2O_3 sample was too weak to be properly displayed, we magnified the intensity by the factor 5.

As references, a pure Sm_2O_3, synthesized by the same sol-gel method, and a NiO sample, prepared by decomposing $Ni(NO_3)_2$*6 H_2O at 873 K for 2 hours, were used. The pure NiO sample shows a clear, distinct peak centered around 655 K, which is close to reported values by e.g. Jankovic et al.[34] The highly loaded samples with 63 wt% and 89 wt% Ni show a similar reduction profile and resemble the profile of pure NiO, although slightly shifted to higher temperatures which might result from the embedment in Sm_2O_3. Similar findings have been reported by Augusto et al.[35] for Ni/CeGd catalysts who argue that, with increasing calcination temperature and increasing metal loading, the reduction profiles become similar to the bulk behavior.[35] At lower loadings, the profiles are less clearly pronounced, exhibiting multiple peaks and shoulders, which

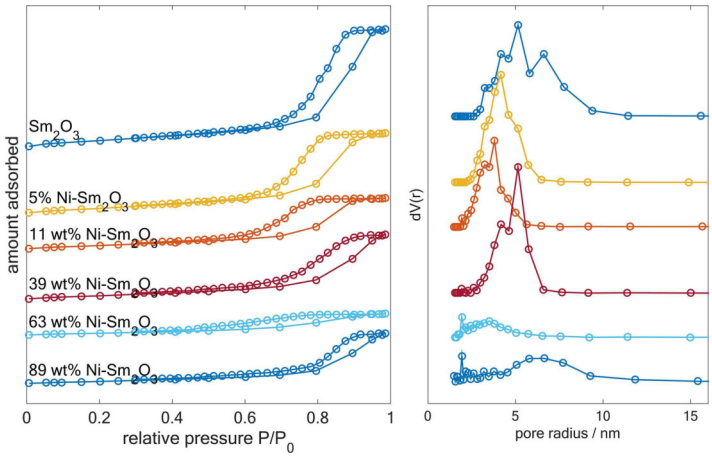

Figure 3. (left) N_2 adsorption/desorption isotherms and (right) pore size distribution as determined by the BJH method of the synthesized xerogels.

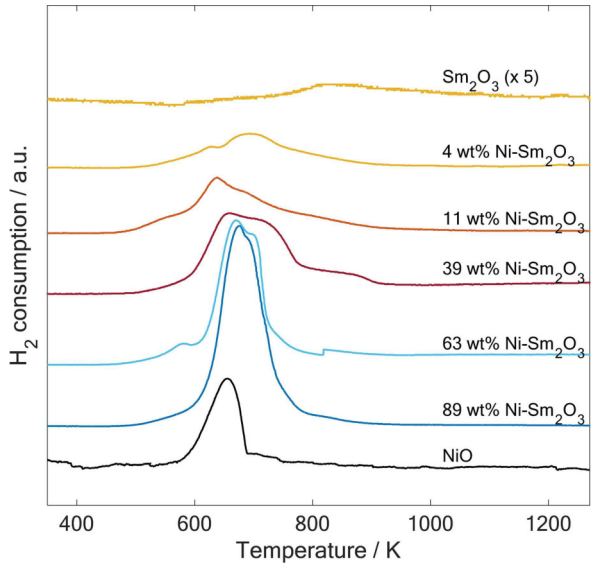

Figure 4. TPR profiles of the synthesized xerogels. Heating ramp: 5 K/min.

are, though, in the same temperature region. As the XRD results reveal the presence of only one NiO species and no mixed oxides, the diffuse profiles indicate the presence of NiO in different chemical environments characterized by a varying interaction with Sm_2O_3.[36,37] Further, the samples show a pronounced tailing, which occurs in the same temperature region as the reduction of the pure Sm_2O_3. Samaria is considered a thermally stable oxide which does not undergo complete reduction; however, it possesses the ability to form oxygen vacancies in a reducing atmosphere at elevated temperatures.[38] We, thus, attribute at least part of the tailing to the formation of oxygen vacancies within the Sm_2O_3 structure.

Catalysis

All catalysts were tested for CO_2 methanation at different temperatures at a weight hourly space velocity (WHSV) of 60 $L_N g_{cat}^{-1} h^{-1}$. Prior to the reaction, the samples were reduced in-situ at 773 K for 10 h under flowing hydrogen. The CO_2 conversion as well as CH_4 selectivity at the investigated temperatures are depicted in Figure 5 for all synthesized catalysts. Generally, the catalysts exhibit an exceptional conversion level, particularly at low and medium temperatures, outperforming the reference kinetics. The samples reported here have a low onset temperature, being already active at 523 K, while the methane selectivity is for all samples and temperatures outstandingly high. Interestingly, the sample with 39 wt% Ni shows the highest conversion level, whereas the catalysts with 63 wt% and 89 wt% Ni perform worse as compared to the 39 wt% sample but are among each other very similar, despite the differing Ni loading. Smaller Ni loadings, in turn, lead to the lowest conversion levels. At high temperatures exceeding 573 K, kinetic limitations, in particular film diffusion, lead to only small increases in conversion, despite drastically higher temperatures. The methane selectivity is close to 100%, independently of the Ni loading. However, with increasing temperature the selectivity is slightly decreasing due to CO formation via the endothermic reverse water-gas shift reaction.

To explain the results, mechanistic as well as morphological reasons appear likely. It is known that CO_2 adsorption takes primarily place at the metal-support interface[6] rendering a pure Ni catalyst inactive for low temperature CO_2 methanation.[39] This is also in accordance with our pre-experiments over unsupported Ni. In case of the catalysts with 63 and 89 wt% Ni loading, the Ni portion of the surface is already very high (in particular when considering the large difference in molar mass of the two components) so that the area for CO_2 adsorption on Sm_2O_3 is presumably rather low. Apparently, the 39 wt% Ni–Sm_2O_3 catalyst offers the best ratio of Sm_2O_3 (CO_2 adsorption) and Ni sites (H_2 adsorption and dissociation) including a high number of perimeter sites. In addition, the

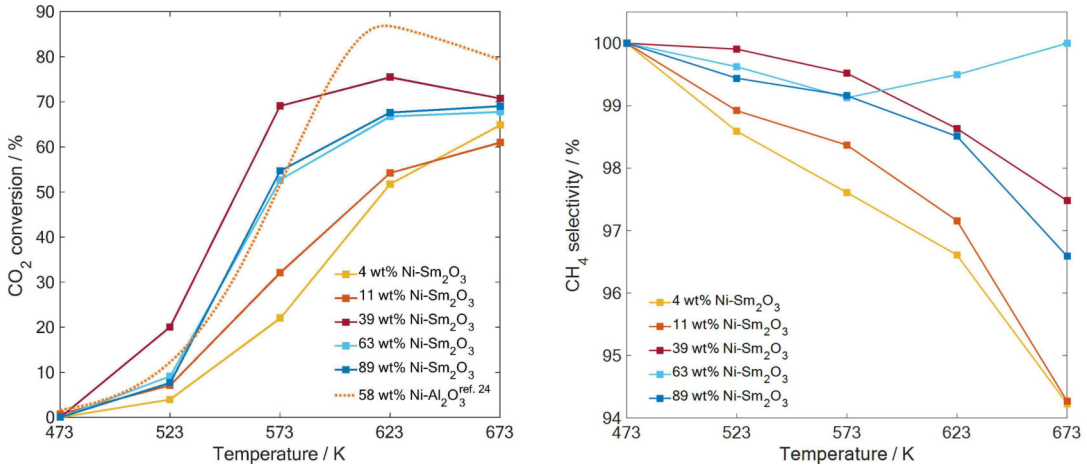

Figure 5. CO_2 conversion (left) and corresponding CH_4 selectivity (right) for various temperatures and Ni loadings. 60 $L_N/(h\,g_{cat})$; feed composition 4/1/5 H_2/CO_2/Ar; reference kinetics adapted from [25].

samples with 63 wt% and 89 wt% Ni loading, have a significantly smaller specific surface area, as discussed before.

Another factor, playing a role, could be the smaller pore radii or larger crystallite sizes in the latter two cases. However, calculating the Weisz-Prater criterion[40] according to Equation (10), in which r^{eff} denotes the observed reaction rate, ρ_{cat} the catalyst density, d_{cat} the particle diameter, c_{CO_2} the inlet CO_2 concentration and and $D^{eff}_{CO_2}$ the effective diffusion coefficient of CO_2 in H_2:

$$WP = \frac{r^{eff}\rho_{cat}d_{cat}^2}{4c_{CO_2}D^{eff}_{CO_2}} < 1 \qquad (10)$$

shows no intra particle diffusion limitations, thus, eliminating the pore size as an influential factor. In contrast, the significantly smaller average crystallite size of 39 wt% Ni–Sm_2O_3 is a likely factor, since small crystallite sizes are considered to be favorable for the activity in structure-sensitive reactions like the CO_2 methanation.[41,42]

In addition, we determined the activation energy for the catalysts with 11 wt%, 39 wt% and 63 wt% Ni for the interval 503 K to 573 K. The corresponding graphs are shown in the SI (Figure S4). We derived activation energies of 82.42 kJ/mol, 81.63 kJ/mol and 83.45 kJ/mol for the catalysts with 11 wt%, 39 wt% and 63 wt% Ni, respectively. The determined activation energies are at the lower end of previously reported values for Ni based systems, however, slightly larger than 77.5 kJ/mol as observed for the reference kinetics. Yang et al.[43] found an activation energy of 95 kJ/mol, whereas others reported values between 80–106 kJ/mol on various Ni based systems.[44,45]

Stability Considerations

One major problem encountered is the fast deactivation of the catalyst as has also been observed by Muroyama et al.,[10] for which they could not find an explanation. Their characterization of the spent catalyst revealed the absence of coking or sintering, though. Figure 6 (top) illustrates the deactivation profile over time for 11 wt% Ni–Sm_2O_3, whereas at the bottom a comparison between the different catalysts is shown. All catalysts exhibit a significant drop in conversion at 573 K over 600 min. Thereafter, a stable operation is possible as the conversion only decreases marginally over the next 1000 min (see Figure 6). Note that the selectivity remains unchanged over the whole measurement period. After applying a re-reduction step in pure H_2 at 763 K (hydrogen bracketing technique), the initial conversion level can be completely restored. Deactivation is independent of the catalyst used, as they all loose about 14% (rel.) of activity over the measurement period; thus, structural changes are unlikely due to the differing morphology of the catalysts. This point is further strengthened by the reversibility of the deactivation as sintering or structural changes are usually irreversible, an assumption which was confirmed by post-catalysis XRD measurements.

Coking would be possible; however, is very unlikely as the CO_2 methanation is not prone to coking and no methane could be observed when re-reducing the catalyst.[3] According to the literature, Ni hydroxide and oxide evolution is also unlikely to form at the applied reaction conditions,[46] although, several studies point out the inhibiting effect of H_2O by blocking adsorption sites.[25,47] It is, however, known that Sm_2O_3 tends to form carbonates which would also deactivate the catalyst reversibly and independently of the metal loading by blocking adsorption sites.

Aldana et al.[6] conducted operando IR spectroscopy measurements on Ni–CeO_2–ZrO_2 catalysts and observed the formation of mono- as well as polydentate carbonates. We, therefore, ran the reaction at elevated CO_2 partial pressures and observed a markedly increased activity loss, and thus, believe that carbonate formation is the predominant deactivation cause. The extent of carbonate formation is, generally, linked to the basicity of the material with weaker basic supports tending to form less carbonates, and thus, being less prone to deactivation

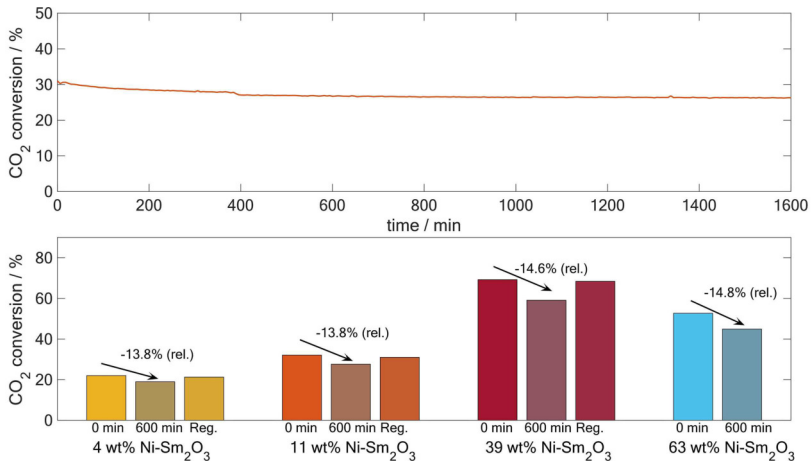

Figure 6. (top) CO_2 conversion over time at 573 K, applied catalyst: 12 wt% Ni–Sm_2O_3 (bottom). Comparison of the CO_2 conversion at 573 K of the pristine catalysts, after 600 min at 573 K as well as after a re-reduction step at 763 K.

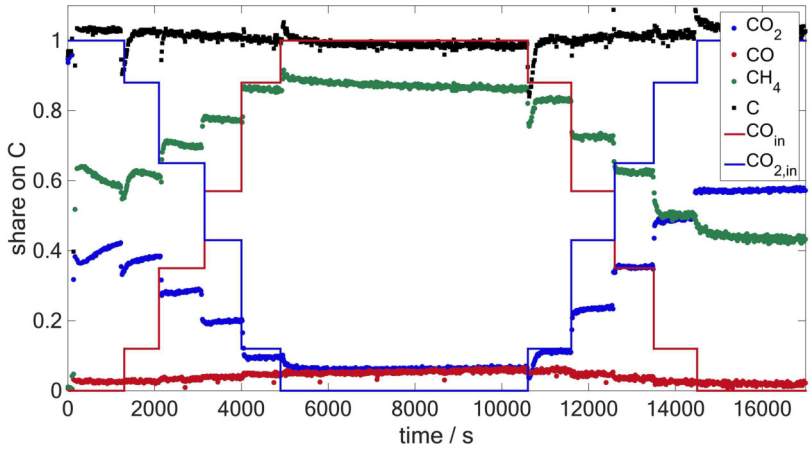

Figure 7. CO_2/CO co-methanation at 573 K; catalyst: 69 wt% Ni–Sm_2O_3 (30 mg), feed: 4/1/1.5 H_2/CO_x/Ar at 50 mL/min. Solid lines indicate feed compositions.

by carbonate formation. This means, that the basicity of the support might play an ambivalent role favoring on the one hand CO_2 adsorption, and therefore, increasing the activity, whereas on the other hand, carbonate formation is enhanced, negatively affecting the catalyst stability. However, these assumptions need to be investigated in more detail, which will be topic of a subsequent paper.

CO_2/CO Methanation

We, further, conducted simultaneous CO_2/CO methanation measurements to evaluate the influence of CO on the catalyst performance as well as to gain insights into the reaction mechanism. Therefore, we adjusted our measurement procedure. The reactor was loaded with 30 mg of 63 wt% Ni–Sm_2O_3. The feed composition was set to 4/1/1.5 H_2/C/Ar at 50 ml/min. The temperature remained fixed at 573 K. The product gas composition was monitored using a quadrupole mass spectrometer (Hiden Analytics) and Ar was used as reference to quantify CO_2, CO and CH_4. The results are given in Figure 7.

The carbon balance was close to 1 at all times. Starting from pure CO_2 methanation, CO_2 was stepwise replaced in the feed with CO as indicated by the solid lines. Once the carbon feed consisted only of CO, CO_2 partial pressure was increased again at the expense of CO. As can be easily seen, no deactivation or poisoning occurs after adding CO to the feed. In fact, methane yield and carbon conversion increase with higher CO share proving the high activity not only for CO_2 but also for CO methanation. The carbon conversion as well as methane yield are maximized under pure CO methanation conditions, whereas they are the lowest under pure CO_2 methanation conditions. The steep decline in CH_4 in the first 1000 s can be attributed to the rapid deactivation as has been discussed previously. It is remarkable that CO conversion is under the present reaction conditions over 90%, while the reverse water-gas shift reaction (RWGS) contributes only little as indicated by the low CO_2 concentration in the product gas. Furthermore, judging from the conversion, CO is converted preferentially over CO_2 to

methane. This indicates that the activation barrier for CO activation is lower compared to the activation of CO_2, which is in agreement with the literature. Kopyscinski et al.[48] found an activation energy for CO methanation of 74.1 kJ/mol which is within the 72–78 kJ/mol interval reported by Gardner and Bartholomew.[49] In opposition, we determined the activation energy for CO_2 methanation at the applied catalyst to be 83.5 kJ/mol, which is in the reported range of 80–106 kJ/mol for different Ni-Al_2O_3 systems.[25,44,45] Inui et al.[50] suggest that the preferential methanation of CO under co methanation conditions results from a stronger adsorption of CO on the surface. Tada and Kikuchi[42] performed a meta study to gain mechanistic insights into the selective methanation of carbon monoxide and developed a mechanism based on numerous literature findings. They assume that CO_2 adsorption takes place on the support to form carbonates, whereas CO and H_2 adsorb on the Ni surface. After the dissociation of H_2, hydrogen either hydrogenates CO adsorbed on the metal or spills over to carbonates on the support to form formates. However, only the formates in close proximity to the metal are subsequently decomposed to CO and further hydrogenated to methane. Unfortunately, the authors elaborate neither on the further steps involved in the hydrogenation of CO, nor on the rate determining step (RDS). If the RDS is not the C–O bond cleavage of the CO intermediate/educt or the conversion of the carbonates proceeds by formaldehyde and methoxy species as suggested by Aldana et al., this mechanism can very well explain the observed lower reaction rate of CO_2, particularly since our results suggest the formation of surface carbonates. While several studies assume that CO_2 conversion takes place once CO has been removed from the feed,[50–52] our results point in the same direction, however, cannot fully confirm this conclusion. We, thus, conclude, that the addition of CO to the feed at least significantly retards CO_2 methanation. The exceptional performance for the simultaneous as well as pure CO methanation proves the suitability of the investigated materials for other catalytical applications such as syngas conversion or efficient CO removal.

Conclusions

A new one-pot synthesis route was applied to synthesize Ni–Sm_2O_3 xerogel catalysts with different Ni loadings which were fully characterized and subsequently tested for CO_2 methanation. Our findings show that an optimal metal loading exists at 39 wt% Ni–Sm_2O_3. This catalyst outperforms even a highly active literature known system proving its potential for CO_2 methanation. Stability tests reveal that deactivation occurs independently of the metal loading to the same extent. The deactivation is, however, completely reversible after applying a re-reduction step and most likely caused by carbonate formation. Furthermore, as shown by the simultaneous CO_2/CO methanation experiments, the catalyst is also highly active for CO methanation at 573 K with a preferential conversion of CO rendering our catalyst suitable for various other application such as syngas conversion as well as selective CO hydrogenation. Future research will be directed to in-depth characterization of the deactivation phenomena and to the improvement of the stability. Since the activity of the samaria supported system outperforms standard catalysts for the hydrogenation of CO_2, Sm_2O_3 supports could be useful for the Fischer-Tropsch synthesis as well.

Conflicts of interest

There are no conflicts to declare.

Acknowledgements

We thank Dr. L Kiewidt (Wageningen University) for the calculations and S. Neumann (University of Bremen) for TEM measurements. JI and MB gratefully acknowledge financial support by the German Research Foundation (DFG) through the graduate school GRK1860 "MIMENIMA – Micro-, meso- and macroporous nonmetallic Materials: Fundamentals and Applications".

Conflict of Interest

The authors declare no conflict of interest.

Keywords: CO methanation · CO_2 methanation · Ni catalyst · rare earth metal oxide catalyst · xerogel catalysts

[1] M. Schubert, S. Pokhrel, A. Thomé, V. Zielasek, T. M. Gesing, F. Roessner, L. Mädler, M. Bäumer, *Catal. Sci. Technol.* **2016**, *6*, 7449–7460.
[2] K. Ghaib, K. Nitz, F. Ben-Fares, *Chem. Biol.* **2016**, *3*, 266–275.
[3] S. Rönsch, J. Schneider, S. Matthischke, M. Schlüter, M. Götz, J. Lefebvre, P. Prabhakaran, S. Bajohr, *Fuel* **2016**, *166*, 276–296.
[4] G. A. Mills, F. W. Steffgen, *Catal. Rev.* **1974**, *8*, 159–210.
[5] K. R. Thampi, J. Kiwi, M. Grätzel, *Nature* **1987**, *327*, 506–508.
[6] P. A. U. Aldana, F. Ocampo, K. Kobl, B. Louis, F. Thibault-Starzyk, M. Daturi, P. Bazin, S. Thomas, A. C. Roger, *Catal. Today* **2013**, *215*, 201–207.
[7] M. Marwood, R. Doepper, A. Renken, *Appl. Catal. A Gen.* **1997**, *151*, 223–246.
[8] B. Miao, S. S. K. Ma, Xi Wang, H. Su, S. H. Chan, *Catal. Sci. Technol.* **2016**, *6*, 4048–4058.
[9] M. Schoder, U. Armbruster, A. Martin, *Chemie-Ingenieur-Technik* **2013**, *85*, 344–352.
[10] H. Muroyama, Y. Tsuda, T. Asakoshi, H. Masitah, T. Okanishi, T. Matsui, K. Eguchi, *J. Catal.* **2016**, *343*, 178–184.
[11] S. Scirè, C. Crisafulli, R. Maggiore, S. Minicò, S. Galvagno, *Catal. Letters* **1998**, *51*, 41–45.
[12] H. Cui, M. Zayat, D. Levy, *J. Non. Cryst. Solids* **2005**, *351*, 2102–2106.
[13] S. Rahmani, M. Rezaei, F. Meshkani, *J. Ind. Eng. Chem.* **2014**, *20*, 4176–4182.
[14] K. Takehira, T. Shishido, P. Wang, T. Kosaka, K. Takaki, *J. Catal.* **2004**, *221*, 43–54.
[15] M. A. O'Brien, PhD thesis, **1997**.
[16] H. Qin, C. Guo, Y. Wu, J. Zhang, *Korean J. Chem. Eng* **2014**, *31*, 1168–1173.
[17] H. Liu, X. Zou, X. Wang, X. Lu, W. Ding, *J. Nat. Gas Chem.*, **2012**, *21*, 703–707.
[18] S. Sato, R. Takahashi, M. Kobune, H. Gotoh, *Appl. Catal. A Gen.* **2009**, *356*, 57–63.

[19] T. Mori, H. Masuda, H. Imai, A. Miyamoto, S. Baba, Y. Murakami, *J. Phys. Chem.* **1982**, *86*, 2753–2760.
[20] S. Tada, T. Shimizu, H. Kameyama, T. Haneda, R. Kikuchi, *Int. J. Hydrogen Energy*, **2012**, *37*, 5527–5531.
[21] L. Atzori, M. G. Cutrufello, D. Meloni, R. Monaci, C. Cannas, D. Gazzoli, M. F. Sini, P. Deiana, E. Rombi, *Int. J. Hydrogen Energy* **2017**, *42*, 20689–20702.
[22] S. Sharma, Z. Hu, P. Zhang, E. W. Mcfarland, H. Metiu, *J. Catal.* **2011**, *278*, 297–309.
[23] M. Schubert, L. Schubert, A. Thomé, L. Kiewidt, C. Rosebrock, J. Thöming, F. Roessner, M. Bäumer, *J. Colloid Interface Sci.* **2016**, *477*, 64–73.
[24] A. E. Gash, T. M. Tillotson, J. H. Satcher, L. W. Hrubesh, R. L. Simpson, *J. Non. Cryst. Solids* **2001**, *285*, 22–28.
[25] F. Koschany, D. Schlereth, O. Hinrichsen, *Appl. Catal. B Environ.* **2016**, *181*, 504–516.
[26] B. J. Clapsaddle, B. Neumann, A. Wittstock, D. W. Sprehn, A. E. Gash, J. H. Satcher, R. L. Simpson, M. Bäumer, *J. Sol-Gel Sci. Technol.* **2012**, *64*, 381–389.
[27] Y. Zhang, *Synth. React. Inorganic, Met. Nano-Metal Chem.* **2016**, *46*, 1565–1570.
[28] H. Yang, H. Wang, H. M. Luo, D. M. Feldmann, P. C. Dowden, R. F. DePaula, Q. X. Jia, *Appl. Phys. Lett.* **2008**, *92*, 062905.
[29] D. R. Lide, 79th ed. CRC, **2009**.
[30] T. F. Baumann, A. E. Gash, S. C. Chinn, A. M. Sawvel, R. S. Maxwell, J. H. Satcher, Jr, **2004**.
[31] B. Neumann, T. W. Elkins, A. E. Gash, H. Hagelin-Weaver, M. Bäumer, *Catal. Letters* **2015**, *145*, 1251–1261.
[32] W. D. Zhang, B. S. Liu, Y. L. Tian, *Catal. Commun.*, **2007**, *8*, 661–667.
[33] L. M. Gomez-Sainero, R. T. Baker, A. J. Vizcaı, S. M. Francis, A. C., I. S. Metcalfe, J. J. Rodriguez, **2009**, 8364–8372.
[34] B. Janković, B. Adnadević, S. Mentus, *Chem. Eng. Sci.* **2008**, *63*, 567–575.
[35] B. L. Augusto, L. O. O. Costa, F. B. Noronha, R. C. Colman, L. V. Mattos, *Int. J. Hydrogen Energy* **2012**, *37*, 12258–12270.
[36] K. Stangeland, D. Y. Kalai, H. Li, Z. Yu, *Appl. Energy* **2018**, *227*, 206–212.
[37] Y. Li, G. Lu, J. Ma, *RSC Adv.* **2014**, *4*, 17420–17428.
[38] J. H. Jhang, A. Schaefer, W. Cartas, S. Epuri, M. Bäumer, J. F. Weaver, *J. Phys. Chem. C* **2013**, *117*, 21396–21406.
[39] P. Riani, G. Garbarino, M. A. Lucchini, F. Canepa, G. Busca, *J. Mol. Catal. A. Chem.* **2014**, *383–384*, 10–16.
[40] P. B. Weisz, C. D. Prater, *Adv. Catal.* **1954**, *6*, 143–196.
[41] M. A. A. Aziz, A. A. Jalil, S. Triwahyono, A. Ahmad, *Green Chem.* **2015**, *17*, 2647–2663.
[42] S. Tada, R. Kikuchi, *Catal. Sci. Technol.* **2015**, *5*, 3061–3070.
[43] J. Yang, J. Mcgregor, A. J. Sederman, J. S. Dennis, *Chemical Engineering Science* **2016**, *141*, 28–45.
[44] T. Van Herwijnen, H. Van Doesburg, W. A. De Jong, *J. Catal.* **1973**, *28*, 391–402.
[45] R. Maatman, S. Hiemstra, *J. Catal.* **1980**, *62*, 349–356.
[46] B. Mutz, A. Gänzler, M. Nachtegaal, O. Müller, R. Frahm, W. Kleist, J. D. Grunwaldt, *Catalysts* **2017**, *7*, 279.
[47] M. A. A. Aziz, A. A. Jalil, S. Triwahyono, M. W. A. Saad, *Chem. Eng. J.* **2014**, *260*, 757–764.
[48] J. Kopyscinski, T. J. Schildhauer, F. Vogel, S. M. A. Biollaz, A. Wokaun, *J. Catal.* **2010**, *271*, 262–279.
[49] D. C. Gardner, C. H. Bartholomew, *Ind. Eng. Chem. Prod. Res. Dev.* **1981**, *20*, 80–87.
[50] T. Inui, M. Funabiki, Y. Takegami, *Ind. Eng. Chem. Prod. Res. Dev.* **1980**, *19*, 385–388.
[51] H. Habazaki, M. Yamasaki, B. P. Zhang, A. Kawashima, S. Kohno, T. Takai, K. Hashimoto, *Appl. Catal. A Gen.* **1998**, *172*, 131–140.
[52] B. Nematollahi, M. Rezaei, E. Nemati Lay, *J. Rare Earths* **2015**, *33*, 619–628.

Manuscript received: January 23, 2019
Revised manuscript received: January 6, 2019
Accepted manuscript online: January 10, 2019
Version of record online: February 22, 2019